Organic Electronics 44 (2017) 132–143

Contents lists available at ScienceDirect

Organic Electronics

journal homepage: www.elsevier.com/locate/orgel

Charge transport in lead sulfide quantum dots/phthalocyanines hybrid nanocomposites

Chandana Pal [a], Lydia Sosa-Vargas [b], Jesús J. Ojeda [a, 1], Ashwani K. Sharma [c], Andrew N. Cammidge [b], Michael J. Cook [b], Asim K. Ray [a, *]

[a] Institute of Materials and Manufacturing, Brunel University London, Uxbridge, Middlesex UB8 3PH, UK
[b] School of Chemistry, University of East Anglia, Norwich NR4 7TJ, UK
[c] United States Air Force Research Laboratory, Space Vehicles Directorate, SE Kirtland AFB, NM 87117, USA

ARTICLE INFO

Article history:
Received 29 December 2016
Received in revised form
10 February 2017
Accepted 11 February 2017
Available online 14 February 2017

Keywords:
Bohr radius
Quantum confinement
Photophysical quenching
Percolation limit
Hopping conduction
Memristors

ABSTRACT

A hybrid composite of non-aggregated lead sulfide (PbS) nanoparticles of average size 5.8 ± 1 nm embedded within a film of an octaalkyl substituted metal-free phthalocyanine (Compound **2**) was prepared on interdigitated gold electrodes by mild acidic treatment of newly synthesised octasubstituted lead phthalocyanine analogue (Compound **1**) in solid state phase. This nanocomposite film shows an enhancement of in-plane electrical conductivity over that of a film of octaalkyl substituted metal-free phthalocyanine alone by nearly 65%. This observation is consistent with the formation of charge complex compound as indicated by Raman and XPS data. The presence of PbS in the composite was examined on the basis of XRD peak positions which are comparable with those of bulk PbS. A band gap of 2.22 eV was calculated from optical absorption data using Tauc's law, implying quantum confinement. The mono dispersal behaviour of PbS nanoparticles was established from TEM and XRD studies. The hopping conduction mechanism is found to be primarily responsible for charge transport in the hybrid nanocomposite film with the hopping distance larger than PbS diameter.

1. Introduction

Hybrid materials containing inorganic nanoparticles in organic matrices have generated enormous fundamental research interest in the field of nanoscience because of their potential applications in environmental, optoelectronic, biomedical and energy storage fields [1]. The conjugated π system of chemically stable, environmentally non-toxic macrocyclic phthalocyanine (Pc) compounds exhibits interesting physical opto-electronic properties leading to a variety of applications in the field of organic electronics [2], energy conversion and storage [3] and biosensors [4]. Similarly, the size-dependent unique opto-electronic properties of crystalline semiconductor quantum dots (QDs) typically made of chalcogenides or phosphides of II to VI metals have attracted active research attention for their applications in nanoelectronics, optics and biological sciences [5]. Therefore, attempts have been made in recent years to extrinsically dope phthalocyanines with inorganic nanoparticles like lead sulphide (PbS), zinc sulphide (ZnS), cadmium sulphide (CdS) and cadmium selenide (CdSe) with a view to developing hybrid photovoltaic cells devices with enhanced performances [6]. The fluorescence intensity for stable hybrid complexes containing CdSe QDs and polycationic aluminium phthalocyanine in aqueous solution was observed to be 48% more than that for only free Pc, an effect leading to possible enhanced photosensitizing activity in photodynamic therapy [7]. The interaction between quantum dots and phthalocyanine conjugates may be of various types such as surface passivation of the matrix by the quantum dots, electrostatic interaction, hydrogen bonding, and Van der Waal bonding. Electron transfer between CdSe acceptor quantum dots and substituted silicon phthalocyanine donor matrix is found from the femtosecond time-resolved spectroscopy to be responsible for improved photophysical activities of CdSe quantum dots inside a substituted silicon phthalocyanine matrix [8]. Cadmium telluride (CdTe) quantum dots capped with thioglycolic acid on positively charged zinc phthalocyanines cause quenching of luminescence intensity of the compound in a solvent mixture of water and pyridine. This phenomenon may be interpreted as fluorescence resonance energy transfer between the electropositive zinc phthalocyanine and CdTe

* Corresponding author.
[1] Present address: Systems and Process Engineering Centre, College of Engineering, Swansea University, Swansea, SA1 8EN, UK.

http://dx.doi.org/10.1016/j.orgel.2017.02.014

[9]. The electrocataytic properties of the conjugations of azide-functionalised CdSe/ZnS QDs with tetrakis (5-hexyn-oxy) iron (II) phthalocynine can be employed for sensing toxic pesticide paraquat with the detection limits of 5.9×10^{-9}μM, satisfying the international standard [10]. The effective non-linear absorption coefficient and free-carrier absorption cross-sections of indium phthalocynine(InPc)/CdSe/ZnS nanocomposites were found to increase with the size of quantum dots and this behaviour is attributed to the increase in photo-excitable free carrier density with increasing CdSe/ZnS QDs radius. These hybrid nanocomposites show threshold limit fluence of 0.77Jcm^{-2} which is at least one order magnitude lower than a value reported for nanocomposites containing InPc and single walled carbon nanotubes [11].

There are several methods described in the literature for the synthesis of nanocomposites [12,13]. Synthesis of PbS nanoparticles is comparatively easier than that of other semiconductors like ZnO, PbSe, CdSe and CdS. This is because of the large exciton Bohr radius (18 nm) of PbS. The Bohr radius of CdS, for example, is 5.4 nm and the confinement effect occurs for the radius less than 2 nm. In addition to this, PbS has a larger band gap than those of the other lead-containing chalcogenides PbSe and PbTe. The size, shape, density of the nanoparticle PbS can be tuned by changing the substrate, temperature, reaction phase and reagent of synthesis and the tuneable property of the PbS quantum dots makes them suitable for use in a broad range of applications, telecommunication to biological imaging [14,15]. The common problem inherent with the solution-phase synthesis is the aggregation of the nano-sized particles due to their high surface energy. The aggregation makes the surface imperfect and also traps the charge carriers resulting in a decrease of mobility [16]. Attempts have been made to overcome these problems by coating the nanoparticles with surfactants. The surfactants prevent the nanoparticles from adhesion by making a physical barrier outside the particles [17]. However, the disadvantage of coating is that the surfactant acts as an insulating layer and affects the charge transport. These difficulties may be overcome by employing in-situ one step solid state a synthetic route by which inorganic quantum dots are embedded in an organic matrix suitable for a specific device application.

Lead phthalocyanine molecules have been reported to have a 'shuttle-cock' like structure with a C_{4v} symmetry and the Pb—N bond length is estimated to vary between 0.22 and 0.24 nm depending upon the substitutions. These distances are smaller than the bond length in a planar phthalocyanine [18]. The out-of-plane Pb atom makes the Pb—N bond weaker and can be easily removed by a reducing agent like hydrogen sulphide (H_2S) gas. This property has been exploited in our previous work for one-step, cost-effective solid state synthesis of inorganic/organic hybrid nanocomposites through the displacement of lead from spin-coated thin films of octahexyl substituted discotic liquid crystalline lead phthalocyanine (6 PbPc) under an atmosphere of hydrogen sulphide to afford PbS quantum dots embedded in a single layered metal free phthalocyanine matrix. The process was considered to be complete over a 24 h period. Also, the aggregation of the quantum dots was avoided to a considerable extent by this solid state synthesis. The size and band gap were estimated as 2.24 nm and 1.91 eV respectively [19]. Subsequent work has established that the lability of lead in a range of octaalkyl substituted phthalocyanines under mild acidic conditions in the solution phase varies according to the chain length. In light of this behaviour, a number of examples of this class of compound has been investigated when formulated as thin films and exposed to H_2S [20]. This establishes that films of the octaoctyl substituted lead phthalocyanine, denoted as 8 PbPc (Compound **2** in Fig. 1), may be more readily converted into the PbS and metal free phthalocyanine C_8H_2Pc analogue (Compound **1**) nanocomposite formulation than 6 PbPc. This enhanced rate of de-metallation reduces formulation time and can be significant if devices are to be prepared for large scale manufacture. Following similar steps, structurally distorted octa-(benzo-15-crown-5)-substituted phthalocyaninato Cd(II) was exploited to form a CdS quantum dots based hybrid/metal-free phthalocyanine [21].

This present article presents the results of comprehensive studies on steady state conduction characteristics of the PbS/C_8H_2Pc nanocomposite on an interdigitated gold electrode system over the temperature range between 87 K and 430 K under a vacuum of 10^{-4} mbar. The presence of PbS in the composite was examined on the basis of XRD peak positions. The hysteresis in the reproducible current-voltage curves is interpreted in the terms of an equivalent circuit as the applied voltage was swept within the voltage range of ±50 V at four different scan rates from 5 mV^{-1} to 5000 mV^{-1}. The sizes of PbS quantum dots have been estimated from the selective-area electron diffraction pattern of TEM studies. Raman and X-ray photoelectron spectroscopy (XPS) data have been analysed to investigate the interaction between PbS and C_8H_2Pc.

2. Experimental

A 50 μl solution of Compound **1** (Fig. 1(a)) in a volatile solvent (99.8% pure toluene from Sigma Aldrich) was dispersed on ultrasonically cleaned substrates for thin film formulation. The choice of the substrates depended upon the type of characterisation experiment undertaken. Silicon wafers were used as substrates for the physical-chemical characterisations of drop cast films which were formed by drying in a vacuum desiccator for at least 4 h. The hybrid nanocomposite films containing PbS quantum dots embedded in an analogue metal free phthalocyanine matrix of Compound **2** were produced by exposing the drop cast films of Compound **1** to H_2S gas (99% purity from Fisher Scientific) for approximately 24 h in a sealed container. Pristine thin films of Compound **2** were also similarly produced on respective substrates for the sake of comparative studies. The main reaction can be presented as

$$C_8PbPc \rightarrow PbS + C_8H_2Pc$$

X-ray diffraction (XRD) patterns of H_2S treated drop cast films of Compound **1** on ultrasonically cleaned silicon wafers were acquired with a Bruker D8 Advance instrument with Bragg-Brentano geometry scanning in the 2θ range of 10° to 60° at the rate of 0.16°/min. The instrument is equipped with CuKα radiation of wavelength λ = 0.154178 nm. XRD measurements were also obtained for galena powder and pristine films of Compound **2.** A Zygo NewView 5000 interferometer with a white laser was used for the thickness measurement. Measurements were repeated on five different areas of the film and an average value of the thickness was used for further analysis. The thickness t of the film is 5 μm. A small amount of drop cast H_2S treated films of Compound **1** was transferred by mechanical scratching from the glass substrate to a copper grid support for transmission electron microscopic (TEM) examinations using a JEOL EM 13005 at an accelerating voltage of 200 kV. In order to determine the thermal stability of H_2S treated films of Compound **1** and Compound **2,** the thermogravimetric analysis (TGA) was carried out on the samples under a nitrogen flow of 50 ml/min using a TA Instruments TGA500. All of the samples were heated up to 700 °C at heating rate of 10 °C/min. Evaluation was carried out using the Universal Analysis 2000 V4.3 software.

A LabRam Raman spectrometer equipped with green an Nd: YAG laser of 613 μW power for excitation at wavelength of 532 nm was employed to study the vibration spectra of similar drop cast samples of H_2S treated Compounds **1** and **2**. The measurements consisted of the acquisition of multiple spectral windows in the

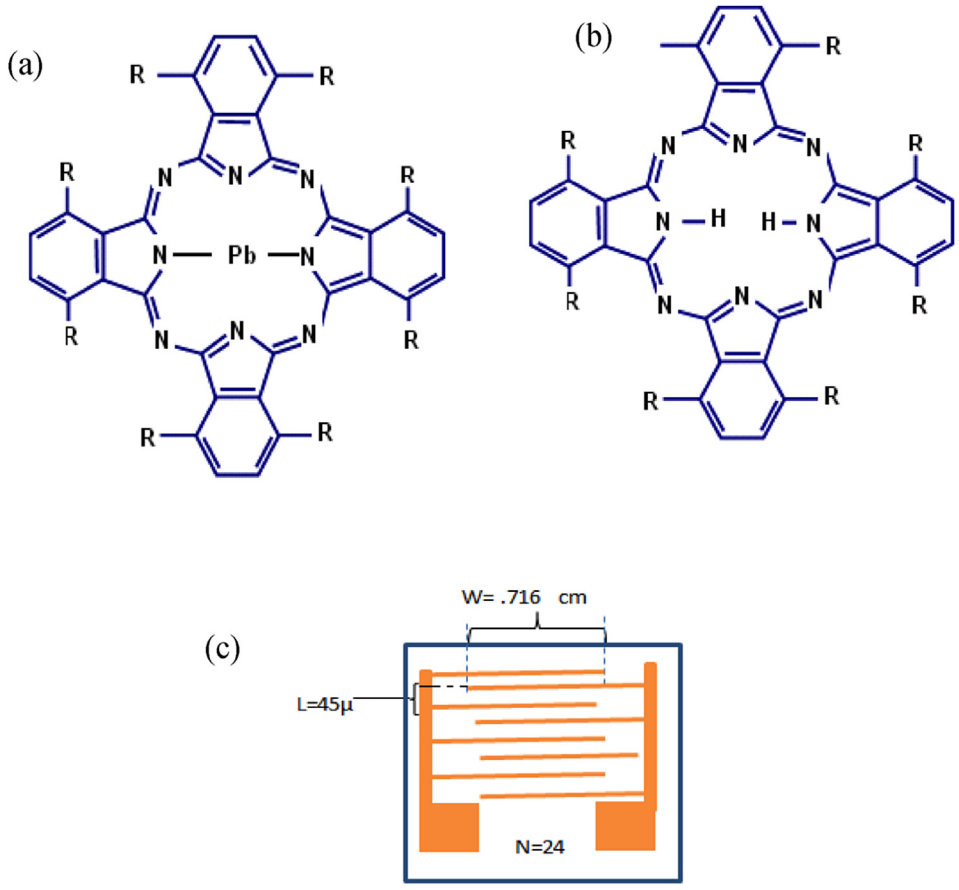

Fig. 1. Structural representation of lead phthalocyanine (Compound **1**) non-peripherically substituted at 1-,4-,8-,11-,15-,18-,22-,25-sites with octakis(octyl) R = C_8H_{17} and (b) 1-, 4-, 8-, 11-, 15-,18-, 22-,25-phthalocyanine metal free (Compound **2**) molecules, (c) interdigitated gold electrodes on glass.

range 500–1700 cm^{-1} (Stokes shifts) with accumulation of 5 scans, each in 30 s. The spectral width is 3 cm^{-1}. Raman spectra were also obtained for H_2S treated films of Compounds **1** and galena powder from 300 to 600 cm^{-1} (40 scans, each in 5 s and spectral width 3.5 cm^{-1}) using the reduced power of 11.8 μW. A Perkin Elmer Spectrum One Fourier Transform Infrared (FTIR) spectrometer with a Specac Golden Gate attenuated total reflection (ATR) accessory collected absorption bands over the 4000 cm^{-1} to 650 cm^{-1} wavenumber range, at a resolution of 4 cm^{-1}. X-Ray photoelectron measurements (XPS) were obtained using a VG ESCALAB 210 Photoelectron Spectrometer. The X-Ray source was a non-monochromatic Al Kα source (1486.6eV), operated with an X-ray emission current of 20 mA and an anode high tension (acceleration voltage) of 12 kV. The takeoff angle was fixed at 90° relative to the sample plane. The area corresponding to each acquisition was of 1 mm^2. Each analysis consisted of a wide survey scan (pass energy 50eV, 1.0eV step size) and high-resolution scans (pass energy 50eV, 0.05eV step size) for component speciation. 10 scans were taken for the survey spectra, and 5 scans were taken for each one of the expansions. The software Casa XPS 2.3.13 was used to fit the XPS spectral peaks. The binding energy scale was calibrated using the Au 4f5/2 (84.0eV), Cu 2p3/2 (932.7 eV) and Ag3d5/2 (368.27 eV) lines of cleaned gold, copper and silver standards from the National Physical Laboratory (NPL), UK. All spectra were charge-corrected to saturated hydrocarbon at 285.0 eV. The photoluminescence excitation and emission spectra were recorded using a Horiba Jobin Yvon Fluorolog-3 spectrofluorometer with a pulsed 450 W Xenon lamp over the wavelength range 365 nm and 800 nm.

Using a KW-4A spin coater from the Chemat Technology Inc., USA, a set of films was deposited for electrical measurements on an interdigitated gold electrode system (Fig. 1(c)) by spinning a 50 μl of the spreading solution at the rate of 1500 rpm for 30 s. A Keithley 617 Programmable electrometer and an Oxford Instrument constant bath liquid nitrogen cryostat were used in a microprocessor controlled measuring system to record current-voltage I(V) characteristics for the samples over the temperature range of 87 K–430 K under a vacuum of 10^{-4} mbar. Optical absorption spectra for similarly spun films on ultrasonically cleaned glass substrates were recorded with a Perkin Elmer LAMBDA 650 UV/Vis spectrophotometer using a 1 cm pathlength cuvette at room temperature with a scanning rate of 654.8 nm/min in the range from 300 nm to 850 nm.

3. Results and discussions

The results of the XRD measurements are summarised in Table 1. The XRD pattern in Fig. 2(a) was obtained for the investigation into structural consequences of exposing drop cast films of Compound **1** to H_2S gas for 24 h. The peak positions at 25.981°, 30.020°, 43.041° and 50.873° are similar to those observed for powdered galena in Fig. 2(b). According to the JCDF cards No. 1-880, these peaks may be identified with the planes (111), (200), (220) and (311) corresponding to d-spacings of 0.34 nm, 0.29 nm, 0.21 nm and 0.18 nm of the face centered cubic lead sulphide (PbS) with the lattice parameter a = 0.593 nm [22]. This value of the lattice parameter a is in good agreement with the value of 0.595 obtained for powdered galena from Fig. 2(b). A comparison with the XRD pattern in Fig. 2(c) for the pristine spun film of Compound **2** implies the

formation of hybrid nanocomposite films containing PbS quantum dots embedded in the matrix of Compound **2** due to the removal of out-of-plane lead atom from Compound **1** by reaction with H_2S. Values of the intensity ratio I_{111}/I_{200} were found to be 0.82 and 0.85 from Fig. 2(a) and (b), respectively. These compare well with the theoretical value of 0.80. The corresponding ratios of I_{220}/I_{200} are, on the other hand, estimated to be 0.40 and 0.63 from Fig. 2(a) and (b), respectively. The comparison with the theoretical ratio of 0.60 implies that the preferred orientation of PbS quantum dots is along the (200) plane [23]. The average size of the PbS particles was estimated from Fig. 2(a) to be 7.1 ± 1.6 nm using the Debye-Scherrer equation [24]. This value is much smaller than its exciton Bohr radius of 18 nm and the threshold size for the quantum confinement is reported to be less than 10 nm for ester capped PbS quantum dots [25]. The broadening of the XRD peaks in Fig. 2(a) is, therefore, believed to be caused by the quantum confinement. Spectra obtained at low angles of incidence, 2θ from 10° to 20°, presented in the inset indicate the structure of the phthalocyanine films [26]. As shown in Inset (i), the ratio of the peaks at 12.6° to one at 13.5° is estimated to be 1 for the pristine film of Compound **2,** whereas this ratio becomes much higher for the nanocomposite film (inset (ii)). The ratios of comparatively low intensity peaks at larger angles are significantly different between the two spectra. This observation is consistent with possible changes in the crystal orientation in the metal-free phthalocyanine matrix, possibly due to the incorporation of PbS in the film [27].

The TEM images in Fig. 3 were recorded for the H_2S treated films of Compound **1**. The dark spots marked in circles in Fig. 3 indicate the presence of PbS quantum dots, showing no obvious aggregation. Their average size was found to be 5.8 ± 1 nm. This value agrees satisfactorily with that previously obtained from XRD within the experimental error. This correlation indicates a good degree of non-aggregation of the PbS quantum dots produced by this method for their synthesis. Values of the interplanar spacing d were estimated to be 0.294 nm and 0.214 nm for the crystal planes (200), (220) using the formula $d = \frac{L\lambda}{R}$ where $L\lambda = 1.9815 \times 10^6$ is known as the camera constant for TEM operating voltage of 200 kV. The distances between the centre spot and the peripheral rings were found to be 6.75 μm and 9.25 μm as the radius R of the selective-area electron diffraction pattern. Both XRD and the selective-area electron diffraction pattern show that PbS quantum dots are polycrystalline. Similar TEM studies have been reported on high temperature solution phase synthesised PbS nanowires and the average diameter size is estimated to be 7 nm which is larger than the value of the present investigation [28].

Thermogravimetric analysis in Fig. 4(a) shows the initiation of thermal decomposition of the H_2S treated films of Compound **1** at 200 °C. Films of Compound **2** in Fig. 4(b), on the other hand, underwent thermal decomposition with an increased mass loss between 364 °C and 442 °C. This thermal behaviour is similar to that reported for a poly[3,6,9-Tris(p-tolylsulfonyl)-3,6,9-triazaundecyl]

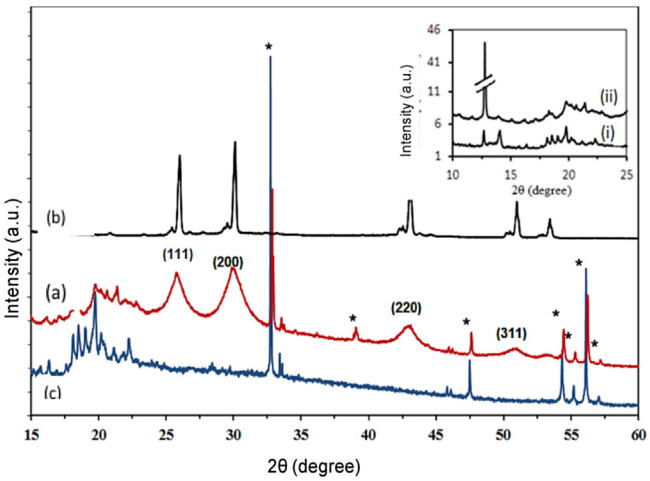

Fig. 2. XRD patterns of (a) H_2S treated film of compound **1**, (b) galena PbS and (c) compound **2**. (inset) (i) compound **2** and (ii) H_2S treated film of compound **1** in the low gazing angle.

{3,6,9-Tris(p-tolylsulfonyl)-1-(3,4-dicyanophenoxy)-3,6,9-triazaundecanyl} metal free phthalocyanine [29]. The residue mass of the hybrid nanocomposite **1** and Compound **2** was found to be 17.2% and 6.1%, respectively at 700°. The PbS content in H_2S treated films is estimated to be 11.1%. This is a reasonable observation in light of the fact that PbS as an ionic compound and has a very high melting point [30]. The volume fraction of PbS quantum dots is estimated to be 2% from the knowledge that the densities of PbS and Compound **2** are 7.60 g/cm^3 and 121 g/cm^3, respectively [31].

The UV–vis spectrum of the H_2S treated film of Compound **1** in Fig. 5(a) exhibits the peak positions of the split phthalocyanine Q band at 763 nm and 640 nm with a shoulder at 688 nm. This absorption behaviour corresponds very well to that observed in Fig. 5(b) for the pristine film of Compound **2**. However, enhanced absorbance was observed in the spectrum of the H_2S treated film of Compound **1** over the wavelength range from 300 nm to 400 nm which is attributable to absorption by lead sulfide. The absorption in PbS in Fig. 5(c) was obtained from the difference between the spectra shown in Fig. 5(a) and 5(b) for the wavelength range between 300 nm and 550 nm displaying the characteristic blue shift of absorption edge with respect to that of the bulk PbS [32]. The Tauc plot of $(Ah\upsilon)^2$ against $h\upsilon$ in the inset was found to be linear, indicating that electronic transitions associated with optical processes is direct [33]. The ratio of the slope to the intercept of the ordinate extrapolated to $h\nu = 0$ produces a value of 2.22 eV for the optical band gap E_{opt} for PbS quantum dots. This value is significantly larger than that obtained for the bulk PbS band gap of 0.41 eV at 298 K with an absorption onset at 3020 nm. This arises

Table 1
d-spacings and lattice indices of dominant reflections and peak orientation as featured in Fig. 2.

2θ (°)		d (nm)		Intensity ratio	
Spun films of Compound **2**	H_2S treated spun films of Compound **1**	Spun films of Compound **2**	H_2S treated spun films of Compound **1**	Spun films of Compound **2**	H_2S treated spun films of Compound **1**
12.40	12.68	0.70	0.69		
13.98	13.29	0.62	0.66	1.00	0.27
18.07	14.51	0.48	0.60	0.83	0.26
18.48	15.85	0.47	0.55	0.89	0.26
19.58	18.21	0.45	0.48	1.09	0.29
19.84	19.68	0.44	0.44	0.85	0.32
21.08	20.11	0.41	0.43	0.76	0.31
22.22	21.31	0.39	0.41	0.84	0.32

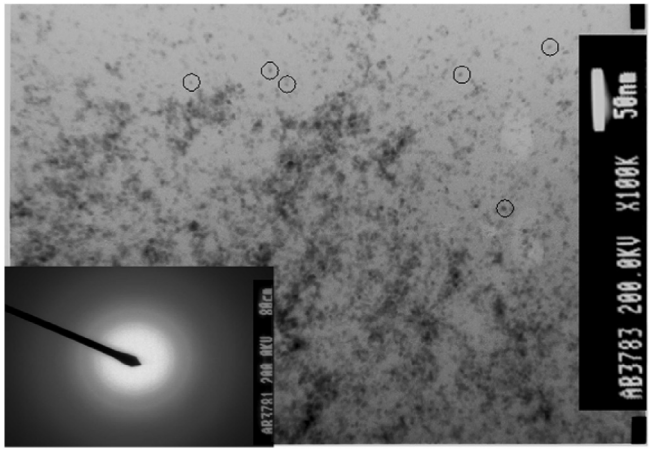

Fig. 3. TEM images of H_2S treated dropcast film of Compound **1** with some of PbS quantum dots marked in circles and selective-area electron diffraction pattern of a PbS quantum dot.

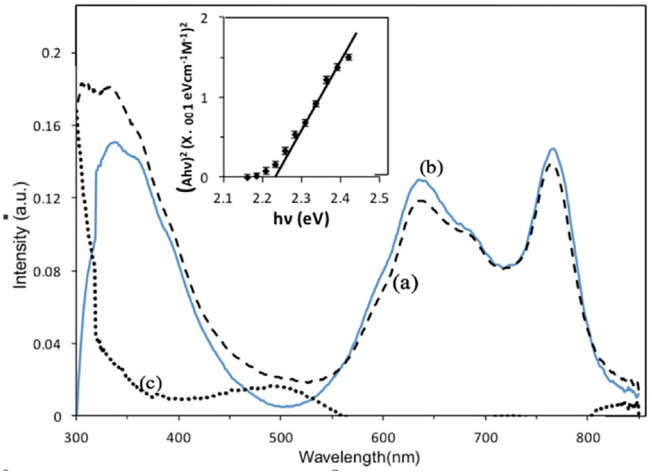

Fig. 5. Optical absorption spectra of (a) H_2S treated spun film of Compound **1** (broken line) (b) spun film of Compound **2** (solid line) (c) PbS after subtracting (dotted line) (a) from (b). (Inset) Tauc plot of $(Ah\nu)^2$ vs hν.

from the quantum confinement of charge carriers in PbS quantum dots with the relatively small effective mass of electrons [34]. E_{opt} is dependent upon the size, stoichiometric ratio and passivating ligands of PbS quantum dots [35].

Raman spectra of drop cast films of both H_2S treated Compound **1** and Compound **2** are presented in Fig. 6(a) and (b) show no appreciable shifts of peak positions between two films. The peak positions with their Raman vibrational assignments of both films are summarised in Table 2 [36,37]. Compound **2** is regarded as being a D_{2h} symmetric molecule. The peaks at 1097 cm^{-1} and 1522 cm^{-1} which remain relatively more defined from adjacent peaks are identified with non-totally symmetric B_{1g} and totally symmetric A_g active modes [37]. A_g modes are not sensitive to charge-transfer effect while B_g modes are highly sensitive to charge-transfer contributions [38]. The relative intensity change between these two peaks is higher for H_2S treated Compound **1** than for Compound **2.** The degree of charge transfer ρ_{CT} was estimated to be 0.29 and 0.39 for Compounds **1** and 2, respectively from the ratio I_R of the intensities of B_{1g} to A_g using the formula

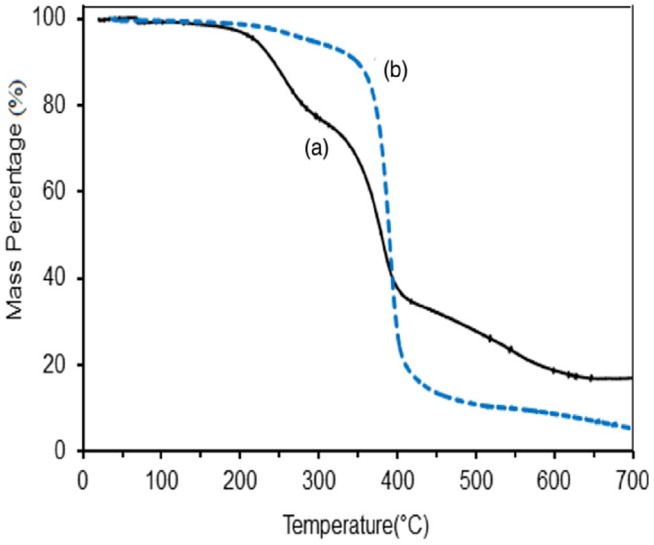

Fig. 4. TGA plots of (a) H_2S treated film of Compound **1** (solid line) and (b) pristine Compound **2** (broken line).

$\rho_{CT} = \frac{I_R}{1+I_R}$. The degree of charge-transfer depends upon the excitation wavelength and the PbS quantum dot size. PbS is a weak Raman scatterer and undergoes degradation under high laser power. A lower scan rate experiment with low laser power was carried out for the Raman band of PbS. The inset of Fig. 6 shows a Raman peak at 480 cm^{-1} for both bulk PbS and PbS quantum dots. This peak is attributed to the vibration of longitudinal optical phonons [39]. FTIR **s**pectra of the films of Compound **2** and H_2S treated Compound **1** are shown in Fig. 7 over the range 650–4000 cm-1. C_8H_2Pc displays 71 infra-red active modes corresponding to D_{2h} symmetry including B_{3u}, B_{2u} term symbols with most intense peaks. Vibrational assignment and symmetry associated with the peaks have been summarised in Table 2 [40]. The peaks in the range 670–1700 cm^{-1} are mostly due to C-C and C-H and N-H vibrations. The peak at 3299 cm^{-1} is assigned as N-H stretching which is absent in metallated phthalocyanines.

XPS data in Fig. 8 show a complex structure of three peaks corresponding to different atomic orbitals. The binding energies were estimated from Fig. 8(a) to be 138.7eV and 143.4eV for $Pb4f_{7/2}$ and $Pb4f_{5/2}$ orbitals respectively for PbS within the spun films of H_2S treated Compound **1.** Fig. 8(b) shows the binding energy of $S2p_{3/2}$ 159.5 eV and $S2p_{1/2}$ at 162.8 eV. Similar values were obtained for PbS quantum dots produced by precipitation of methanolic lead acetate–thiourea [41]. These values also compare well with the

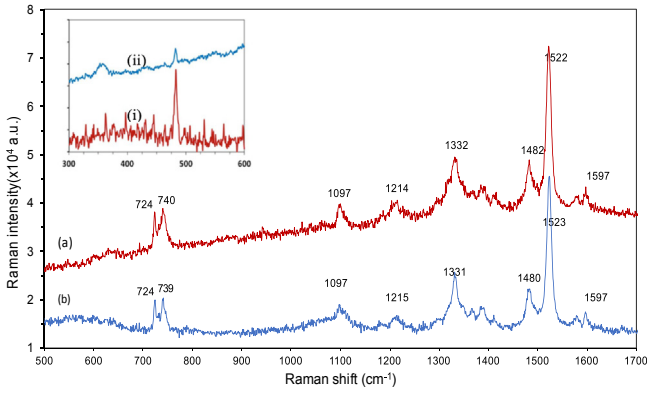

Fig. 6. Raman spectra of (a) H_2S treated film of Compound **1** (b) Compound **2**. (inset) (i) Galena (ii) H_2S treated Compound **1**.

Table 2
Raman shifts (cm^{-1}) for Raman spectroscopy with different laser intensities at 532 nm illustrated in Fig. 6, showing the main peaks and featured FTIR Absorption bands (cm^{-1}) of FTIR pattern illustrated in Fig. 7.

Raman				FTIR			
Compound **2**	H_2S Treated Compound **1**	Vibrational assignment	Symmetry	Compound **2**	H_2S Treated Compound **1**	Vibrational assignment	Symmetry
724	724	Pc ring def.	A_g	750	750	N-H out of plane bending	B_{2u}
739	740	Pc ring def.	A_g	874	874	C-H out of plane def.	B_{3u}
1097	1097	C-H def.	B_{1g}	1023	1023	N-H bending, Isoindole def.	B_{3u}
1215	1214	C-H def.	B_{1g}	1150	1150	C-N, C-H bending in plane	B_{2u}
1331	1332	Pyrrole str.	A_g	1298	1298	–	–
1480	1482	Pyrrole and isoindole str.	A_g	1328	1328	C-C vibr. In isoindole	B_{2u}
1523	1522	Isoindole str.	A_g	1609	1609	C-C str. in pyrrole	B_{3u}
1597	1597	Benzene str.	A_g	3299	3299	N-H str.	B_{3u}

corresponding standard values of 137.2 eV and 142.1eV for Pb4f including 159.2 and 161.9 for S2p in case of bulk galena [42]. The peaks of Pb4f and S2p show an increase of binding energy compared to the bulk PbS. The broad peak at around 169 eV in Fig. 8(b) can be associated to the presence of sulphur dioxide (SO_2) on the surface [19]. The binding energy of the N1s signal of the organic component of H_2S treated Compound **1** in Fig. 8(c) was found to be 399.6 eV, slightly higher than 398.4 eV obtained for Compound **2**. The higher binding energies of the Pb4f, S2p and N1s orbitals compared to the pure components support the conclusion from Raman spectroscopy regarding the charge transfer between the nanocomposite components [37].

Fig. 9(a) shows the photoluminescence (PL) emission spectra of the drop cast films of pristine Compound **2** and H_2S treated Compound **1** in the range 365–800 nm at excitation wavelength 300 nm. Three emission bands were observed at around 446 nm, 662 nm and 776 nm for the film of Compound **2.** The position and relative intensities of these PL bands correlate well with the corresponding phthalocyanine B and Q absorption bands respectively [43]. However, the presence of a single band at 380 nm with splitting and the disappearance of the 662 nm and 776 nm bands were observed for the film of H_2S treated Compound **1**. Plots in Fig. 9(b) of PL spectra were obtained for Compound **2** as a solution in toluene at concentrations from 0.007 mg/ml to 0.7 mg/ml. In comparison to the solid phase, two broad and blue-shifted PL emission bands at 345 nm and 745 and became broader, undergoing greater quenching with rise in concentration. The latter can be attributed to increasing aggregation of the Pc molecules [44]. Also, it can be suggested that the splitting in the 300–400 nm emission bands appears in the presence of less aggregated species

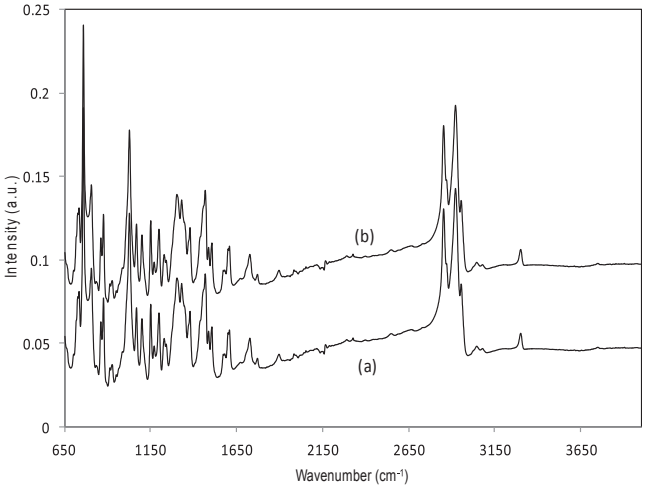

Fig. 7. FTIR spectra of (a) H_2S treated film of Compound **1**, (b) Compound **2**.

or monomers. From the solution phase study, the splitting in the H_2S treated Compound 1 in Fig. 9(a) of thin film spectra can be attributed to the less Pc-Pc interaction of the incorporated PbS quantum dots in the Pc matrix (Fig. 9(b)).

Fig. 10(a) shows a set of reproducible room temperature current-voltage [$I(V_a)$] characteristics of spin coated films of H_2S treated Compound **1** deposited on interdigitated gold electrodes when the applied voltage V_a was swept over the voltage range of ±50 V at four different scan rates from 5 mV^{-1} to 5000 mV^{-1}. In all cases, the direction of the current in the forward voltage sweep (0 V → 50 V and −50 V → 0 V) is reversed in the backward sweep (0 V ← 50 V and −50 V ← 0 V), and shows a scan rate dependent hysteresis. For the sake of clarity, the forward characteristics are given in Fig. 10(b), showing a rise in current with increasing scan rate for the forward applied voltage V_a. The current level is, however, of the same order of magnitude as one obtained for Langmuir-Blodgett films of bis-hydroxyl hexaoctyl metal free phthalocyanine [45]. Measurements were also performed on the spin coated films of Compound **2** in a similar device configuration and the results are shown in Fig. 10(c) for the scan rate of 500 mV^{-1}. Values of room temperature in = plane Ohmic conductivities (σ_x), were estimated to be 1.66 μSm^{-1} and 2.74 μSm^{-1} for Compound **2** and H_2S treated Compound **1**, respectively, using Equation (1) in the form:

$$\sigma_x \approx \frac{I}{V_a}\frac{L(N-1)}{Wt} \quad (1)$$

where values of L and W are indicated in Fig. 1(d). N = 24 is the number of fingers in the electrode system and the thickness t of the thin film is 20 nm. The PbS QDs act as preferential acceptor centres of electrons while the C_8H_2Pc donor molecules provide the supply of electrons. Electrons are progressively transferred to PbS QDs from adjacent C_8H_2Pc molecules under the influence of the applied voltage and remain trapped therein. This charge transfer leads to a significant increase in the density of the majority carriers (holes) in the C_8H_2Pc matrix. As a result, the nanocomposite film of Compound **2** is formed into a complete charge transfer complex after the application of a positive bias voltage with simultaneous reduction in recombination probability for both types of carriers [46]. This gives rise to an increase in conductivity by a factor of 2 for nanocomposite film of Compound **2.**

The hysteresis is found to be more pronounced in the [I (V_a)] characteristic of H_2S treated films of Compound **1** than films of Compound **2**. The effect of the scan rate on the planar charge transport in both films can be interpreted in an equivalent circuit model. The circuit consists of two passive electrical components, resistor R and capacitor C, connected in parallel. The net current I is the sum of the circulating current and displacement components in the form:

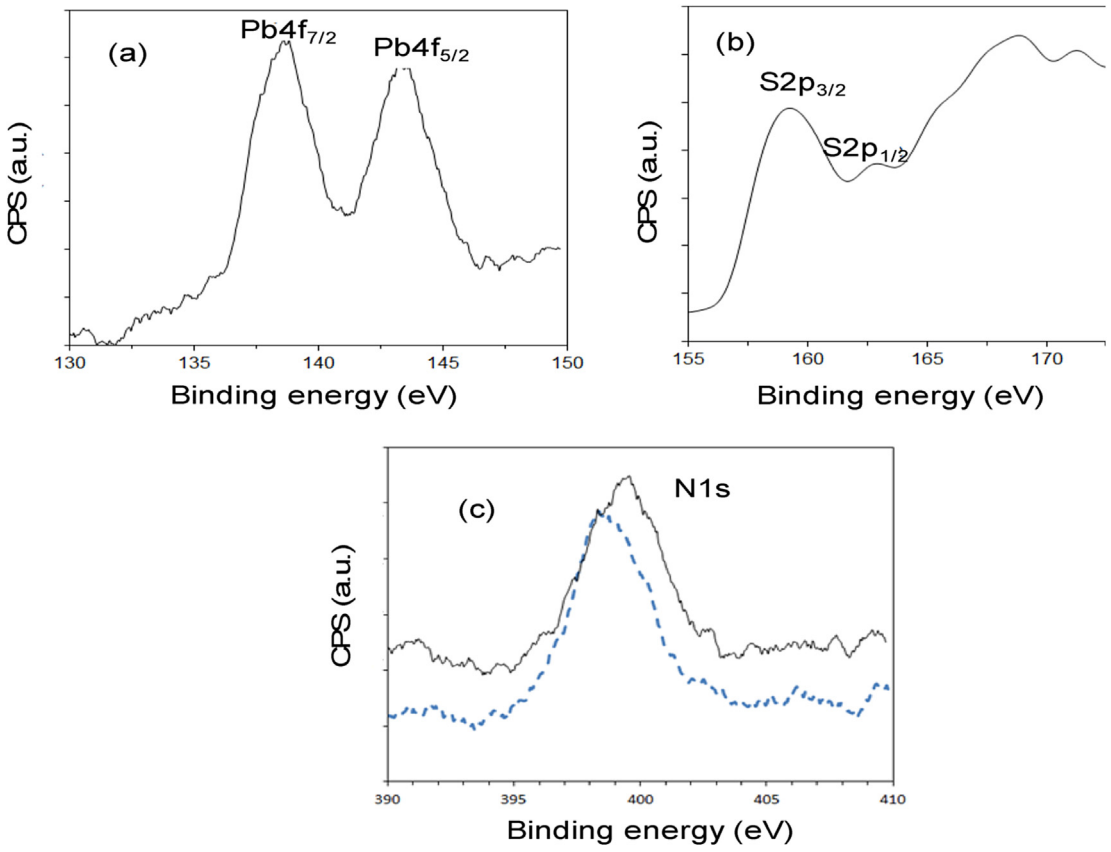

Fig. 8. XPS spectra of (a) Pb4f orbital of PbS QDs; (b) S2P orbital of PbS QDs and (c) N1S orbital of H_2S treated Compound **1** (solid line) and compound **2** (dash line).

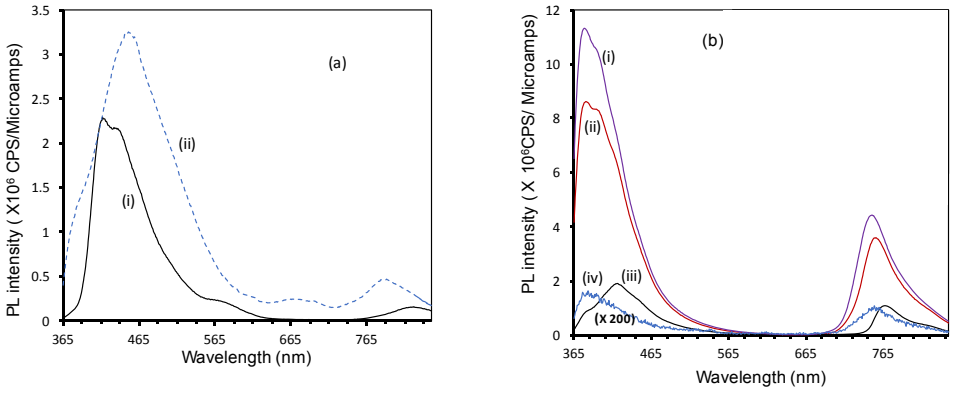

Fig. 9. (a) (i) PL emission spectra of the film of H_2S treated Compound **1** (solid line) and (ii) Compound **2** (dash line); (b) PL emission spectra of solution of Compound **2** in toluene at different concentration in $mgml^{-1}$ (i) 0.007, (ii) 0.018, (iii) 0.071, (iv) 0.600. Excitation wavelength is 300 nm.

$$I = \frac{V_a}{R} + \frac{dV_a}{dt}\left[V_a\frac{dC}{dV_a} + \frac{\tau}{R}\right] \quad (2)$$

where, $\tau = CR$ is the charging and discharging time constant.

Fig. 11 shows the dependence of the short circuit current I_{sc}, open circuit voltage V_{oc} and the hysteresis loop on the scan rate of the applied voltage V_a. The open circuit voltage V_{oc} can be written as $V_{oc} = -\left[\frac{\frac{\tau}{R}\frac{dV_a}{dt}}{\frac{1}{R}+\frac{dV_a}{dt}\frac{dC}{dV_a}}\right]$ for $I = 0$. The gold forms an Ohmic contact with metal free phthalocyanine [47] and the value of the capacitance C may thus be taken to be determined by the geometry, dimension and dielectric constant of the compounds, making $\frac{dC}{dV_a} = 0$. Therefore, the linear rise of V_{oc} with the scan rate in Fig. 11(a) is expected from Equation (2). The linear increase of I_{sc} with the scan rate $\left(\frac{dV_a}{dt}\right)$ in Fig. 11(a) for both samples is in keeping with the observation from Equation (2) that $I_{sc} = \frac{\tau}{R}\frac{dV_a}{dt}$ corresponding to $V_a = 0$. Values of time constant τ for films of H_2S treated Compound **1** and Compound **2** are estimated to be 95s and 75s from the slopes of the graphs. The area of the hysteresis loop is determined by the numerical integration and its value also increases with the scan rate as shown in Fig. 11(c) for both types of film. The sweeping time decreases with the increasing scan rate

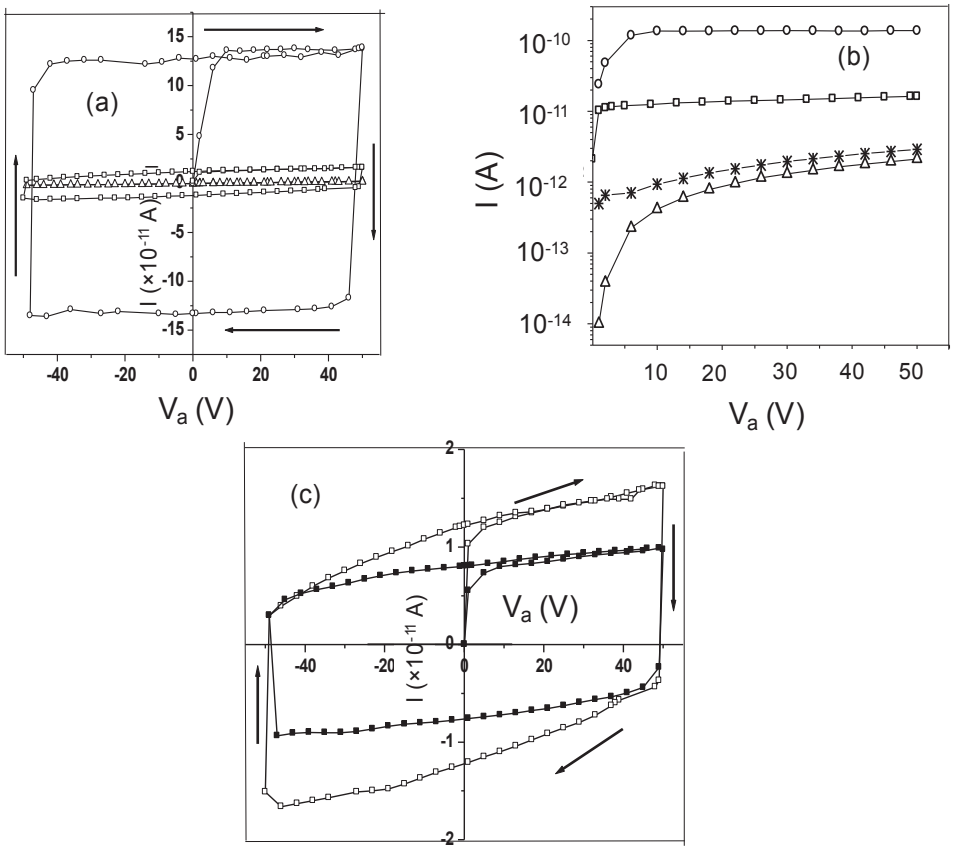

Fig. 10. (a) Current vs applied voltage [I(V_a)] graphs of H_2S treated compound **1** as the applied voltage V_a is swept from 0 V to 50 V in the forward and backward directions at the scan rate of 5 mV^{-1} (triangle), 500 mV^{-1} (square) and 5000 mV^{-1} (circle), arrows show the voltage sweep; (b) Forward [I(V_a)] characteristics of H_2S treated compound **1** at the scan rate of 5 mV^{-1} (triangle), 50 mV^{-1}(star), 500 mV^{-1} (square) and 5000 mV^{-1} (circle); (c) Current vs voltage [I(V_a)] of H_2S treated compound **1** (open square) and compound **2** (solid square) for 500 mV^{-1}, arrows show the voltage sweep.

and this time for the fast scan rates becomes shorter than the time constant τ. Under these circumstances, the majority of the carriers are swiftly swept from the injecting gold electrode finger to the counter electrode contributing largely to the circulating current $\frac{V_a}{R}$. The trap-detrapping mechanisms become progressively slow as the scan rate is increased.

The percolation is not believed to be not responsible for overall planar conduction in view of volume fraction of 2% PBS from the earlier TGA observation [48]. Measurements of the current voltage-characteristics were, therefore, made over the temperature range from 87 K to 430 K for both of H_2S treated films of Compound **1** and Compound **2** with a view to identify the carrier transport mechanism. It is evident from the Arrhenius plot in Fig. 12(a), representing the dependence of lnI on T^{-1}, that no single mechanism is responsible for charge transport over the entire temperature range. Three distinct temperature regimes, namely (i) 87 K ≤ T ≤ 220 K, (ii) 235 K ≤ T ≤ 302 K and (iii) T > 302 K are observed in Fig. 12(a) for H_2S treated films of Compound **1**. The slopes of the linear graphs in Fig. 12(b) give the value of 1.11 meV for the activation energy corresponding to the regime (i) for H_2S treated films of Compound **1** and 2.23 meV for Compound **2** in the same temperature range. Low activation energies of the compounds in the regime (i) imply temperature independent tunnelling conduction through the wall between the localized sites separated by a distance S_0. The tunnelling current can be derived from the following current-temperature relationship (Equation (3)), under the thermally assisted coincidence of the states with activation energy U [49],

$$I = \frac{WtV_a}{L(N-1)} T^{-1} \exp\left[-\left(2\alpha S_0 + \frac{U}{kT} - \frac{2\alpha^2 kT}{m\omega^2} \right) \right] \quad (3)$$

where, $\omega = 10^{12}$ S^{-1}, the frequency of the barrier oscillation; m is the mass with the value of 10^{-25} kg. At very low temperatures the activation energy to cross the barrier is comparatively higher than the thermal energy at that temperature ($U \gg k_B T$). Therefore, the current I_{Tun} is dependent only on the extent of overlap between the wavefunctions ($2\alpha S_0$) and the tunnelling term, $\left(\frac{2\alpha^2 k}{m\omega^2}\right)$. From the linear plot of $\ln(I_{Tun}T)$ vs T in Fig. 12(c), the inverse of site localisation parameter α for the penetration of wave functions into a classically forbidden region was estimated as 0.53×10^8 cm^{-1} for both of H_2S treated Compound **1** and Compound **2**. The intercept of the graphs can be written as $\left(ln \frac{WtV_a}{L(N-1)} - 2\alpha S_0 \right)$. From the value of α, the S_0 was calculated as 8.28×10^{-8} cm for both of H_2S treated Compound **1** and Compound **2.** S_o was taken as independent of temperature and thermal expansion is negligible. The values of α and S_0 are comparable with the values predicted by in Tregold Model for low conductivity semiconductors [50].

As shown in Fig. 13(a), charge transport in H_2S treated Compound **1** in the temperature range (ii) corresponding to 235 K ≤ T ≤ 302 K was identified with the variable range hopping mechanism according to the law in the form of Equation (4) [50]:

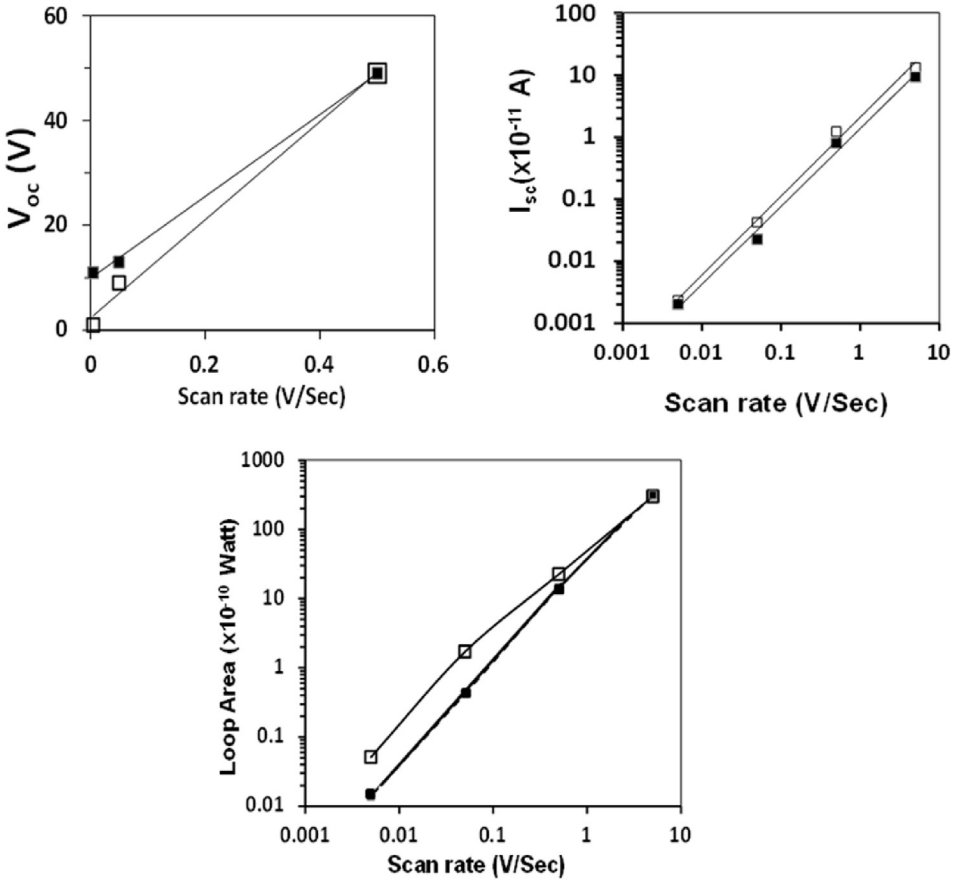

Fig. 11. Dependence of (a) open circuit voltage short circuit current, (b) open circuit voltage and (c) area of hysteresis loop with scan rate for H_2S treated compound **1** (open squares) and compound **2** (solid squares).

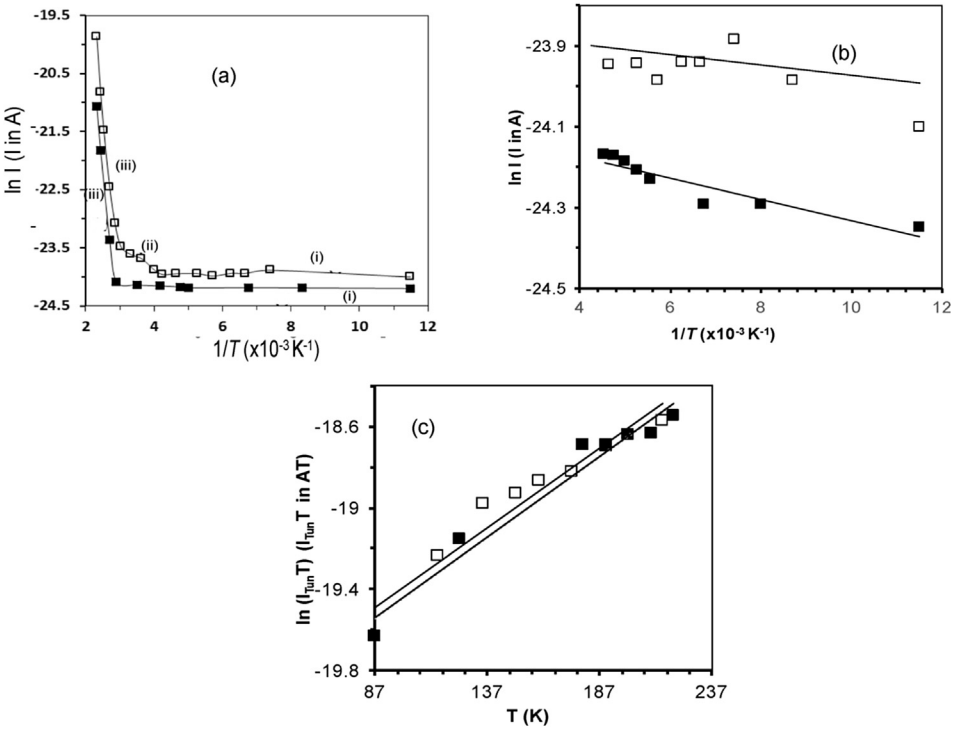

Fig. 12. (a) ln I vs 1/T in the range of temperature 87 K-430 K for (b) Zoomed plot of ln *I* versus 1/*T* in the temperature range 87 K-220 K for H2S treated compound **1** and compound **2** (c) ln (ITunT vs T plot for H2S treated compound **1** and compound **2**. H2S treated compound **1** is represented in open square and compound **2** in closed square. The applied voltage is 50 V.

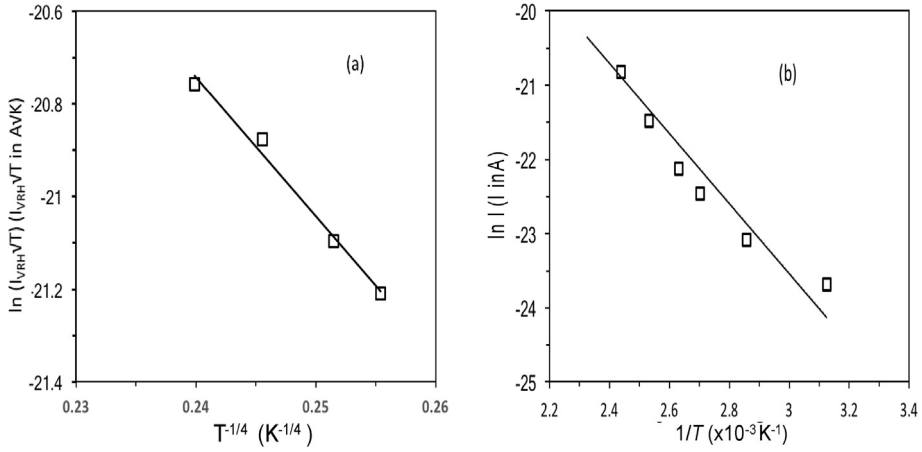

Fig. 13. (a) $\ln(I_{VRH}\sqrt{T})$ vs $T^{-1/4}$ for H_2S treated compound **1** in the temperature range 235 K-302 K, (b) ln I versus 1/T in the range of temperature 320 K-430 K for H_2S treated compound **1**. The applied voltage is 50 V.

$$I_{VRH} = \frac{3WtV_a\upsilon_{ph}\,e^2}{L(N-1)}\sqrt{\frac{9N_0}{8\pi\alpha kT}}\;e^{\left(\frac{T_0}{T}\right)^{1/4}} \quad (4)$$

where, $T_0 = \frac{16\alpha^3}{kN_0}$. The parameter υ_{ph} is called Debye frequency, the average phonon frequency and its value is equal to 10^{13} Hz. The terms T_0 is the characteristic temperature, N_0 is the density of localized states at the Fermi level. Employing Equation (4), the slope of the graph ln $I_{VRH}\sqrt{T}$ vs $T^{-1/4}$ can be expressed as $(T_0)^{1/4}$. The value of intercept is $\ln\frac{3WtV_a\upsilon_{ph}\,e^2}{L(N-1)} + \frac{1}{2}\ln\left(\frac{9N_0}{8\pi\alpha k}\right)$. Using the above Equation (4), the value of T_0 , α and N_0 were measured as 8.10×10^5 K, 1.08×10^7 cm^{-1} and 6.12×10^{20} eV^{-1} cm^{-3} from Fig. 13(a). The optimum hopping distance S_H was found to be 9.05 nm from the knowledge [50] that

$$S_H = \left(\frac{9}{8\pi\alpha kN_0T}\right)^{\frac{1}{4}} \quad (5)$$

In Fig. 13(b), ln *I* versus 1/*T* was plotted corresponding to the region (iii) for H_2S treated Compound **1** of plot 12(a). A sharp rise of current can be observed with changing the temperature from 320 K to 430 K. This activation energy is related to the charge carrier transition between band edges. The activation energy for the conduction was calculated as 0.41 eV using the Arrhenius equation. Hopping conduction was observed in hybrid nanocomposites such as polyaniline titanium dioxide nanocomposites [51]. However, the interpretation of the mechanism in this present investigation has been supported by providing quantitative values of Mott parameters T_0, α, N_0 and S_H.

4. Conclusions

PbS quantum dots of an average size of 5.8 nm and band gap of 2.22 eV were successfully embedded in metal free phthalocyanine (Compound **2**) matrix exploiting the non-planar structure of Compound **1**. The XRD and TEM studies confirmed the presence of PbS QDs. The particle size estimated from TEM is in good agreement with one obtained from XRD study. The volume fraction was estimated as 2% in the matrix, eliminating the possibly of percolation limited conduction involving quantum dots. Photophysical quenching was found in the presence of quantum dots, indicating the incorporation of the QDs in the lattice structure of Compound **2**. Charge transport in the H_2S treated quantum dots obeys the $T^{-1/4}$ law of the variable range hopping mechanism at room temperature. The hopping distance of charge was estimated to 9.05 nm by temperature study of I-V characteristics. In the case of H_2S treated Compound **1**, this value is larger than the percolation limit 5.8 nm for PbS QDs. At very low temperatures isoenergic tunnelling of charges takes place with temperature independent I-V characteristics. The memory behaviour of the metal free phthalocyanine/PbS nanocomposite was studied by the hysteresis in the current-voltage obtained at different scan rates. As the memory loop was found to decrease with the decreasing scan rate, the effect was attributed to trapping and detrapping mechanisms. The gap between the particles may have contributed to the displacement current in the hysteresis loop by trapping and de-trapping of charge. This behaviour of the nanocomposite compound has potential application in memristors.

Acknowledgements

This work is sponsored by the Air Force Office of Scientific Research, Air Force Material Command, USAF, under Grant No. FA9550-15-1-0123.

References

[1] (a) S. Kango, S. Kalia, P. Thakur, B. Kumari, D. Pathania, Semiconductor–polymer hybrid materials, Adv. Polym. Sci. 267 (2015) 283–312, http://dx.doi.org/10.1007/12_2014_295;
(b) K. RoyChoudhury, D.W. Song, F. So, Efficient solution-processed hybrid polymer–nanocrystal near infrared light-emitting devices, Org. Electron. 11 (1) (2010) 23–28, http://dx.doi.org/10.1016/j.orgel.2009.09.017.
[2] O.A. Melville, H.B. Lessard, T.P. Bender, Phthalocyanine based organic thin-film transistors: a review of recent advances, ACS Appl. Mater. Interfaces 7 (24) (2015) 13105–13118, http://dx.doi.org/10.1021/acsami.5b01718.
[3] (a) P. Chawla, M. Tripathi, Novel improvements in the sensitizers of dye-sensitized solar cells for enhancement in efficiency—a review, Int. J. Energy Res. 39 (12) (2015) 1579–1596, http://dx.doi.org/10.1002/er.3366;
(b) F.J. Ramos, M. Ince, M. Urbani, A. Abate, M. Gratzel, S. Ahmad, T. Torres, M.K. Nazeeruddin, Non-aggregated Zn (ii) octa (2, 6-diphenylphenoxy) phthalocyanine as a hole transporting material for efficient perovskite solar cells, Dalton Trans. 44 (23) (2015) 10847–10851, http://dx.doi.org/10.1039/C5DT00396B;
(c) K.S. Lokesh, A. Adriaens, Electropolymerization of palladium tetraaminephthalocyanine: characterization and supercapacitance behaviour, Dyes Pigment. 112 (2015) 192–200, http://dx.doi.org/10.1016/j.dyepig.2014.06.034.
[4] (a) J.F. van Staden, Application of phthalocyanines in flow-and sequential-injection analysis and microfluidics systems: a review, Talanta 139 (2015) 75–88, http://dx.doi.org/10.1016/j.talanta.2015.02.026;
(b) H.H. Wang, Y. Bu, W.L. Dai, K. Li, H.D. Wang, X. Zuo, Well-dispersed cobalt

phthalocyanine nanorods on graphene for the electrochemical detection of hydrogen peroxide and glucose sensing, Sens. Actuator B-Chem. 216 (2015) 298–306, http://dx.doi.org/10.1016/j.snb.2015.04.044.
[5] (a) S. Silvi, A. Credi, Luminescent sensors based on quantum dot–molecule conjugates, Chem. Soc. Rev. 44 (13) (2015) 4275–4289, http://dx.doi.org/10.1039/C4CS00400K;
(b) M. Green, Semiconductor quantum dots: organometallic and inorganic synthesis, RSC Nanosci. Nanotechnol. (2014), http://dx.doi.org/10.1039/9781782628354;
(c) E.H. Sargent, Infrared quantum dots, Adv. Mater. 17 (2005) 515–522, http://dx.doi.org/10.1002/adma.200401552.
[6] (a) B. Lukose, P. Clancy, A feasibility study of unconventional planar ligand spacers in chalcogenide nanocrystals, Phys. Chem. Chem. Phys. 18 (2016) 13781–13793, http://dx.doi.org/10.1039/C5CP07521A;
(b) V.M. Blas-Ferrando, J. Ortiz, V. González-Pedro, R. Sánchez, I. Mora-Sero, F. Fernandez-Lazaro, A. Sastre-Santos, Photovoltaics: synergistic interaction of dyes and semiconductor quantum dots for advanced cascade cosensitized solar cells, Adv. Funct. Mater. 25 (21) (2015) 3220–3226, http://dx.doi.org/10.1002/adfm.201570143.
[7] C. Tshangana, T. Nyokong, The photophysical properties of multi-functional quantum dots-magnetic nanoparticles—indium octacarboxyphthalocyanine nanocomposite, J. Fluoresc. 25 (1) (2015) 199–210, http://dx.doi.org/10.1007/s10895-014-1497-6.
[8] S. Dayal, Y.B. Lou, A.C.S. Samia, J.C. Berlin, M.E. Kenney, C. Burda, Observation of non-förster-type energy-transfer behavior in quantum dot-phthalocyanine conjugates, J. Am. Chem. Soc. 128 (43) (2006) 13974–13975, http://dx.doi.org/10.1021/ja063415e.
[9] S. Moeno, T. Nyokong, Opposing responses elicited by positively charged phthalocyanines in the presence of CdTe quantum dots, J. Photochem. Photobiol. A-Chem. 201 (2–3) (2009) 228–236, http://dx.doi.org/10.1016/j.jphotochem.2008.10.027.
[10] S.R. Nxele, T. Nyokong, Conjugation of azide-functionalised CdSe/ZnS quantum dots with tetrakis (5-hexyn-oxy) Fe (ii) phthalocyanine via click chemistry for electrocatalysis, Electrochim. Acta 194 (2016) 26–39, http://dx.doi.org/10.1016/j.electacta.2016.01.234.
[11] K. Sanusi, T. Nyokong, Indium phthalocyanine–cdse/Zns quantum dots nanocomposites showing size dependent and near ideal optical limiting behaviour, Opt. Mater. 38 (2014) 17–23, http://dx.doi.org/10.1016/j.optmat.2014.09.021.
[12] E.A. Lewis, P.D. McNaughter, Z.J. Yin, Y.Q. Chen, J.R. Brent, S.A. Saah, J. Raftery, J.A.M. Awudza, M.A. Malik, M.P. O'Brien, S.J. Haigh, In situ synthesis of pbs nanocrystals in polymer thin films from lead (ii) Xanthate and dithiocarbamate complexes: evidence for size and morphology control, Chem. Mat. 27 (6) (2015) 2127–2136, http://dx.doi.org/10.1021/cm504765z.
[13] L.T. Yuan, L. Pan, K. Jia, Y.Y. Liu, Z.F. Huang, Y.M. Huang, X.B. Liu, Facile fabrication of white-emitting hybrid colloids and nanocomposite films using cdse/cds quantum dots and zinc phthalocyanines as building blocks, Synth. Met. 218 (2016) 9–18, http://dx.doi.org/10.1016/j.synthmet. 2016.04.030.
[14] S.A. McDonald, G. Konstantatos, S.G. Zhang, P.W. Cyr, E.J.D. Klem, L. Levina, E.H. Sargent, Solution-processed pbs quantum dot infrared photodetectors and photovoltaics, Nat. Mater. 4 (2) (2005) 138–142, http://dx.doi.org/10.1038/nmat1299.
[15] J. Sun, M. Zhu, K. Fu, N. Lewinski, R.A. Drezek, Lead sulfide near-infrared quantum dot bioconjugates for targeted molecular imaging, Int. J. Nanomed. 2 (2) (2007) 235–240.
[16] D.Y. Godovsky, Device applications of polymer-nanocomposites, Adv. Polym. Sci. 153 (2000) 163–205.
[17] W. Wang, Y. Liu, Y. Zhan, C. Zheng, G. Wang, A novel and simple one-step solid-state reaction for the synthesis of pbs nanoparticles in the presence of a suitable surfactant, Mater. Res. Bull. 36 (11) (2001) 1977–1984, http://dx.doi.org/10.1016/S0025-5408(01)00678-X.
[18] D. Atilla, A.G. Gürek, T.V. Basova, V.G. Kiselev, A. Hassan, L.A. Sheludyakovab, V. Ahsen, The synthesis and characterization of novel mesomorphic octa- and tetra-alkylthio-substituted lead phthalocyanines and their films, Dyes Pigment. 88 (3) (2011) 280–289, http://dx.doi.org/10.1016/j.dyepig.2010.07.007.
[19] A.V. Nabok, A.K. Ray, M.J. Cook, P.M. Burnham, Y.H. Iwantono, M. Simmonds, T.V. Basova, Lead sulphide/phthalocyanine nanocomposite spun films, IEEE Trans. Nanotechnol. 3 (3) (2004) 388–394, http://dx.doi.org/10.1109/-TNANO.2004.834155.
[20] L.X. Sosa-Vargas, I. Chambrier, C.J. MacDonald, S.J. Coles, G.J. Tizzard, A.N. Cammidge, M.J. Cook, Synthesis and characterization of some octaalkyl substituted lead phthalocyanines and unexpected variations in lead lability arising from the position of substituents and their chain length, J. Porphyr. Phthalocyanines 17 (6–7) (2013) 511–521, http://dx.doi.org/10.1142/S108842461350020X.
[21] T.V. Basova, N.M. Kurochkina, A.Y. Tsivadze, A.K. Ray, formation of hybrid inorganic/organic nanocomposites, J. Electron. Mater. 39 (2) (2010) 145–148, http://dx.doi.org/10.1007/s11664-009-1024-8.
[22] (a) D. Saikia, P.K. Gogoi, P.K. Saikia, S. Sarma, Synthesis of polymer–pbs nanocomposite by solar irradiation-induced thermolysis process and its photovoltaic applications, J. Exp. Nanosci. 8 (3) (2013) 403–411, http://dx.doi.org/10.1080/17458080.2012.740639;
(b) A.O. Nejo, A.A. Nejo, R.V.S.R. Pullabhotla, N. Revaprasadu, Facile synthesis of organically capped pbs nanoparticles, J. Alloy. Compd. 537 (2012) 19–23, http://dx.doi.org/10.1016/j.jallcom.2012.05.019;
(c) D.D. Liang, S.S. Tang, J.B. Liu, J.H. Liu, X.L. Lv, L.J. Kang, Large scale hydrothermal synthesis of pbs nanorods, Mater. Lett. 62 (15) (2008) 2426–2429, http://dx.doi.org/10.1016/j.matlet.2007.12.012.
[23] (a) S. Seghaier, N. Kamoun, R. Brini, A.B. Amara, Structural and optical properties of pbs thin films deposited by chemical bath deposition, Mater. Chem. Phys. 97 (1) (2006) 71–83, http://dx.doi.org/10.1016/j.matchemphys.2005.07.061;
(b) S.H. Yang, S.H. Wang, K.K. Fung, One-dimensional growth of rock-salt pbs nanocrystals mediated by surfactant/polymer templates, Pure Appl. Chem. 72 (1–2) (2000) 119–126, http://dx.doi.org/10.1351/pac200072010119.
[24] B.D. Cullity, S.R. Stock, Elements of X-ray Diffraction, third ed., Prentice – Hall International, Upper Saddle River, N.J, 2001.
[25] (a) J.C. Liu, H.Z. Yu, Z.L. Wu, W.L. Wang, J.B. Peng, Y. Cao, Size-tunable near-infrared pbs nanoparticles synthesized from lead carboxylate and sulfur with oleylamine as stabilizer, Nanotechnology 19 (34) (2008) 3456021–3456026, http://dx.doi.org/10.1088/0957-4484/19/34/345602;
(b) S.Q. Song, Q.M. Gao, Nanoscience and Technology, in: C. Bai, S. Xie, X. Zhu (Eds.), Pts 1 and 2 Book Series: SOLID State Phenomena, vols. 121–123, 2007, pp. 1305–1308. DOI: 10.4028/, www.scientific.net/SSP.121-123.1305.
[26] (a) Q. Zhang, H.B. Chen, Y.G. Liu, D.Y. Huang, Study on the transformation of metal-free phthalocyanine polymorph crystals by organic solvent treatment, Dyes Pigment. 63 (1) (2004) 11–16, http://dx.doi.org/10.1016/j.dyepig.2003.12.012;
(b) S.M. Bayliss, S. Heutz, G. Rumbles, T.S. Jones, Thin film properties and surface morphology of metal free phthalocyanine films grown by organic molecular beam deposition, PCCP Phys. Chem. Chem. Phys. 1 (15) (1999) 3673–3676, http://dx.doi.org/10.1039/A904089G.
[27] D.W. Deng, J. Cao, J.F. Xia, Z.Y. Qian, Y.Q. Gu, Z.Z. Gu, W.J. Akers, Two-phase approach to high-quality, oil-soluble, near-infrared-emitting PbS quantum dots by using various water-soluble anion precursors, Eur. J. Inorg. Chem. 15 (2011) 2422–2432. DOI:10.1 002/ejic. 2011 00012.
[28] Z. Wang, B. Zhao, F. Zhang, W. Mao, G. Qian, X.P. Fan, Novel single-crystal pbs nanowires directed by [200], Mater. Lett. 61 (17) (2007) 3733–3735, http://dx.doi.org/10.1016/j.matlet.2006.12.085.
[29] A. Bilgin, C. Yagci, U. Yildiz, E. Ozkazanc, E. Tarcan, Synthesis, characterization, aggregation and thermal properties of a novel polymeric metal-free phthalocyanine and its metal complexes, Polyhedron 28 (11) (2009) 2268–2276, http://dx.doi.org/10.1016/j.poly.2009.04.026.
[30] K.T. Wheeler, D. Walker, M.C. Johnson, Galena stability to 26 kbar, Am. J. Sc. 307 (2007) 590–611, http://dx.doi.org/10.2475/03.2007.02.
[31] K. RoyChoudhury, M. Samoc, A. Patra, P.N. Prasad, Charge carrier transport in poly (N-Vinylcarbazole): cds quantum dot hybrid nanocomposite, J. Phys. Chem. B 108 (5) (2004) 1556–1562, http://dx.doi.org/10.1021/jp0360671.
[32] A.D. Yoffe, Semiconductor Quantum Dots and Related systems: electronic, optical, luminescence and related properties of low dimensional systems, Adv. Phys. 50 (1) (2001) 1–208, http://dx.doi.org/10.1080/00018730010006608.
[33] A.K. Ray, C.A. Hogarth, On the analysis of experimental data for optical absorption in non-crystalline materials, J. Phys. D-Appl. Phys. 23 (4) (1990) 458–459, http://dx.doi.org/10.1088/0022-3727/23/4/012.
[34] B. Zhang, G.H. Li, J. Zhang, Y. Zhang, L.D. Zhang, Synthesis and characterization of pbs nanocrystals in water/C12e9/cyclohexane microemulsions, Nanotechnology 14 (4) (2003) 443–446, http://dx.doi.org/10.1088/0957-4484/14/4/307.
[35] (a) I. Moreels, K. Lambert, D. Smeets, D. De Muynck, T. Nollet, J.C. Martins, F. Vanhaecke, A. Vantomme, C. Delerue, G. Allan, Z. Hens, Size-dependent optical properties of colloidal PbS quantum dots, ACS Nano. 3 (10) (2009), http://dx.doi.org/10.1021/nn900863a, 3023–3010;
(b) L. Cademartiri, E. Montanari, G. Calestani, A. Migliori, A. Guagliardi, G.A. Ozin, Size-dependent extinction coefficients of pbs quantum dots, J. Am. Chem. Soc. 128 (31) (2006) 10337–10346, http://dx.doi.org/10.1021/ja063166u;
(c) D. Kim, D.H. Kim, J.H. Lee, J.C. Grossman, Impact of stoichiometry on the electronic structure of pbs quantum dots, Phys. Rev. Lett. 110 (19) (2013) 1968021–1968025, http://dx.doi.org/10.1103/PhysRevLett.110.196802.
[36] C. Murray, N. Dozova, J.G. McCaffrey, S. FitzGerald, N. Shafizadeh, C. Crepin, Infra-red and raman spectroscopy of free-base and zinc phthalocyanines isolated in matrices, Phys. Chem. Chem. Phys. 12 (35) (2010) 10406–10442, http://dx.doi.org/10.1039/c0cp00055h.
[37] R. Aroca, D.P. Dilella, R. Loutfy, J. Phys. Chem. Solids 43 (8) (1982) 707–711, http://dx.doi.org/10.1016/0022 -3697(82)90235-9;
(b) A. Zhong, Y. Zhang, Y. Bian, Structures and spectroscopic properties of nonperipherally and peripherally substituted metal-free phthalocyanines: a substitution effect study based on density functional theory calculations, J. Mol. Graph. Model. 29 (3) (2010) 470–480, http://dx.doi.org/10.1016/j.jmgm.2010.09.003.
[38] X.Q. Fu, Y. Pan, X. Wang, J.R. Lombardi, Quantum confinement effects on charge-transfer between pbs quantum dots and 4-mercaptopyridine, J. Chem. Phys. 134 (2) (2011) 0247071–0247075, http://dx.doi.org/10.1063/1.3523646.
[39] K.S. Upadhyaya, M. Yadav, G.K. Upadhyaya, Lattice dynamics of iv–VI ionic semiconductors: an application to lead chalcogenides, Phys. Stat. Sol. (B) 229 (3) (2002) 1129–1138, http://dx.doi.org/10.1002/15213951-(200202)229:3<1129::AID-PSSB1129>3.0.CO;2–6.
[40] X.X. Zhang, Y.X. Zhang, J.Z. Jiang, Isotope effect in the infrared spectra of free-

base phthalocyanine and its N, N-Dideuterio-Derivative: density functional calculations, Vib. Spec. 33 (1–2) (2003) 153–161, http://dx.doi.org/10.1016/j.vibspec.2003.08.001.

[41] J.D. Patel, F. Mighri, A. Ajji, T.K. Chaudhuri, Morphology and size control of lead sulphide nanoparticles produced using methanolic lead acetate trihydrate–thiourea complex via different precipitation techniques, Mater. Chem. Phys. 132 (2–3) (2012) 747–755, http://dx.doi.org/10.1016/j.matchemphys.2011.12.006.

[42] C.D. Wagner, W.M. Riggs, L.E. Davis, J.F. Moulder, in: G.M. Muilenberg (Ed.), Handbook of X-Ray Photoelectron Spectroscopy, Perkin Elmer Corporation, USA, 1979.

[43] (a) X. Sun, C.Q. Ma, J.Z. Jiang, Luminescence and photophysics of sandwich-type bis(phthalocyaninato) europium compound, Synth. Met. 139 (2) (2003) 497–500. DOI: 0.1016/S0379-6779(03)00206-6.;
(b) K. Yoshino, S.B. Lee, T. Sonoda, H. Kawagishi, R. Hidayat, K. Nakayama, M. Ozaki, K. Ban, K. Nishizawa, K. Ohta, H. Shirai, Optical properties of substituted phthalocyanine rare-earth metal complexes, J. Appl. Phys. 88 (12) (2000) 7137–7143, http://dx.doi.org/10.1063/1.1316050.

[44] W.F. Freyer, C.C. Neacsu, M.B. Raschke, Absorption, luminescence, and raman spectroscopic properties of thin films of benzo-annelated metal-free porphyrazines, J. Lumin. 128 (4) (2008) 661–672, http://dx.doi.org/10.1016/j.jlumin.2007.11.070.

[45] A.K. Ray, A. Nabok, A.K. Hassan, M.J. Cook, Photoconduction in langmuir-blodgett films of octasubstituted metal-free phthalocyanine molecules, IEE Proc.-Circuit Device Syst. 146 (1) (1999) 44–48, http://dx.doi.org/10.1049/ip-cds:19990268.

[46] Z. Khozaee, L. Sosa-Vargas, A.N. Cammidge, M.J. Cook, A.K. Ray, Hybrid phthalocyanine/lead sulphide nanocomposite for bistable memory switches, Mater. Res. Express 2 (9) (2015) 96305–96328, http://dx.doi.org/10.1088/2053-1591/2/9/096305.

[47] F.R. Fan, L.R. Faulkner, J. Chem. Phys. 69 (7) (1978) 3334–3338, http://dx.doi.org/10.1063/1.436987.

[48] L. Bakueva, S. Musikhin, E.H. Sargent, H.E. Ruda, A. Shik, in: H.S. Nalwa (Ed.), Luminescence and Photovoltaic Effects in Polymer-based Nanocomposites Handbook of Organic–Inorganic Hybrid Materials and Nanocomposites, vol. 2, 2003, p. 181 (American Scientific).

[49] C.M. Hurd, Quantum tunnelling and the temperature dependent DC conduction in low-conductivity semiconductors, J. Phys. C Solid. State. 18 (35) (1985) 6487–6499, http://dx.doi.org/10.1088/0022-3719/18/35/014.

[50] N.F. Mott, E.A. Davis, Electronic Processes in Non-crystalline Materials, Clarendon, Oxford, 1971.

[51] A. Dey, S. De, A. De, S.K. De, Characterization and dielectric properties of polyaniline-TiO_2 nanocomposites, Nanotechnology. 15 (9) (2004) 1277–1283.